International Journal of Engineering Research in Africa
ISSN: 1663-4144, Vol. 59, pp 205-223

Submitted: 2021-01-31
Revised: 2021-09-13
Accepted: 2021-09-16
Online: 2022-03-15

Numerical Simulation and Experimental Study of Natural Convection Flow in a Test Bench for Solar Air Heaters

Badis Bakri[1,a*], Hani Benguesmia[2,3,b], Ahmed Ketata[4,c], Slah Driss[4,d] and Zied Driss[4,e]

[1]Mechanical Department, Faculty of Technology, M'sila University, M'sila, Algeria

[2]Electrical Engineering Laboratory (LGE), University of M'sila, M'sila, Algeria.

[3]Department of Electrical Engineering, Faculty of Technology, University of M'sila, M'sila, Algeria

[4]Laboratory of Electromechanical Systems (LASEM), National School of Engineers of Sfax (ENIS), University of Sfax, Sfax, Tunisia

[a*]badis.bakri@univ-msila.dz, [b]hani.benguesmia@univ-msila.dz,[c]ketata.ahmed.enib@gmail.com, [d]slah.driss@gmail.com, [e]zied.driss@enis.tn

Keywords: Solar air heaters, test bench, two air passages, box prototype, aerodynamic structure.

Abstract. This paper is intended to check the thermal convection flow during a new solar air heater (*SAH*) test bench, which is conducted in the LASEM laboratory. In fact, the applied system includes two-passage heater solar air separated by an absorber. On the other hand, a glass piece is connected to the box prototype via a pipe. Then, the piece of the glass is attached to the front side of this device in which an absorber is inserted. Moreover, two circular holes are made on the same face of the box prototype. The first is an entry hole through which hot air goes inside, and an exit hole through which air is released into the surrounding area. The study was conducted using the Navier-Stokes equations associated with the k–ω turbulence model through the use of the newly released Ansys *17.0* software to characterize the aero-thermal structure of our new system operating in natural convection. In these conditions, it has been observed that the hot zone created on the mirror side receiving the solar radiation generates an ascendant movement. It goes from the bottom to the top and enters the box prototype. The same phenomenon is also created in the box where the airflow coming from the solar heat escapes into the environment. This movement created between the hot zone of the solar heat and the box prototype is also imposed in the cold zone of the solar heat on the heat-insulating side. In these conditions, the air movement is however from the top to the bottom. Indeed, the acceleration of the air velocity at the inlet of the solar heat is due to the change of the section which is more reduced by comparison to the rest of the air circulation duct. Based on our experimental results generated in a two-passage solar air heater connected to the box prototype, the computational approach and the simulation results were validated. By referring to the classic solar air heater with one passage, the energy efficiency measured in the same conditions was enhanced and presented the efficient one with an improvement of about *27%*. Finally, the numerical results are compared to our experimental results and those obtained by the authors. The comparison proved a good agreement.

Introduction

The use of solar energy is commonly considered by designers and therefore has been the subject of much research [1-5]. For instance, Pandey et al. [6] a newly proposed type of external pneumatic vortex fog curtain dust removal device installed on road header makes the combination of droplets and dust more closely and effectively prevents the diffusion of dust. For their part, Singh et al. [7] significant changes were observed in the heat transfer rate, the heat transfer in magneto hydro dynamic slip flow of an incompressible, viscous, electrically conducting, forced convective, and steady alumina-water nanofluid in the presence of a magnetic field over a flat plate has been analyzed. Moreover, numerical flow measurement in an enclosure with different dome configurations was developed based on a finite element method. In fact, a numerical analysis of the

natural convection flow was conducted by Bocu and Altac [8] in rectangular enclosures with pins. For his part, El-Sebaiietal [9] contrasted the temperatures of the outlet air and the absorber layer for the double-pass solar air heater configuration with the corrugated layer. His findings showed that the second design is more effective than the first. On the other hand, Wazed et al. [10] contrasted the forced and natural circulation of air in the solar air heater. As for Sopian et al. [11] they confirmed that adding porous media improves the efficiency of a double-pass solar collector. In fact, their experimental validation showed that the theoretical simulation was in close agreement with the experimental results. For their part, Esen et al. [12] conducted an experimental analysis on a solar air heater with and without obstacles while the optimum value of efficiency was obtained for a double-flow collector with obstacles. On the other hand, Ozgen et al. [13] examined a system for the use of an aluminum cans absorbing plate for a solar air heater. The maximum efficiency was achieved for a mass flow rate of *0.05 kg/s*. Then, Theodosius et al. [14] presented an experimental-numeric comparison to give the precision of the CFD model. Driss et al. [15] studied the aerodynamic components of a building system fitted with a solar patio. In fact, these systems can boost the building's microclimate. In another research study, Driss et al. [16] suggested an acceptable building environment to boost thermal comfort. In another study, Joshi et al. [17] introduced the idea of the double-pass *SAH* by confirming that a typical system is more effective than a single-pass one. As for Hassen et al. [18] they analyzed the efficiency of the *SAH* double-pass system with different absorber plate configurations. Based on the results obtained after a number of experimental tests, Allamet al. [19] verified that the double pass of the *SAH* system achieves better outputs than the single-pass one. For their part, Goodarzi et al. [20] stated that the wall temperature in the double-pass heat exchanger is more uniform than normal. In this context, Singh and Dhiman [21] suggested that the use of the double-pass *SAH* system significantly improves the thermal efficiency compared to the other considered device. Then, Chen and Zhang [22] examined the basic characteristics of solar thermal conversion using supercritical CO2-dimethyl ether (DME) natural convection. The authors found that the implementation of the DME successfully reduced the operational pressure and that the rise in the DME fraction contributed to further reductions. Besides, the basic characteristics of the solar thermal conversion using supercritical CO2 natural convection were proposed by Zhang et al. [23]. The writers found that the collection efficiency rises with a comprehensive coefficient, which is a trend contrary to that of the water-based method. As for Chen and Zhang [24] they tested a novel solar thermal conversion and water heater device achieved by supercritical natural CO2 circulation. The writers revealed that the supercritical flow of the CO2 pipe with Reynolds can be greater than *6700* and that the temperature of the CO2 fluid in the heat exchanger can be as high as 80°C. On the other hand, Essen et al. [25] proposed a model for the prediction of the efficiency of the *SAH* system by using the process of the least square support vector machine (LS-SVM). The basic method was intended to control the *SAH* system for efficient modeling. For their part, Essen et al. [26] used both the artificial neural network (ANN) and the wavelet neural network (WNN) to model the current *SAH* system. The efficiency of their proposed approach was evaluated using several statistical validation parameters. In fact, a comparison between the expected and the experimental results suggested that the proposed WNN model could be used to estimate some parameters of the *SAH* system.

As a consequence and based on the literature reviews, we have introduced a new *SAH* system with two passages attached to a box prototype. Unlike other applications, we have incorporated in this system new modifications attaching to the shape design. Particularly, we have considered new dimensions and location of the various compounds, such as the absorber, the collector, the diffuser and the holes. In the present paper, a numerical simulation and experimental validation in our *SAH* test bench are developed. Particularly, we are interested in the study of the aero-thermal structure characterization of our new system operating in natural convection. By referring to the paper of Elsanossi [27] studying the performance of a classic solar air heater with different absorber materials in a single pass, we found that the energy efficiency measured in the same conditions gives enhanced performance and presents the efficient one with an improvement of about *27%.* So,

it is recommended to consider the new proposed design for the improvement of the industrial process.

Solar air heater system (*SAH*)

Figure 1 presents a new solar air heater test bench designed and installed in our LASEM laboratory to investigate the performance of the solar system. The device in question consists of two passages of a solar air heater separated by an absorber.

Fig.1 Box prototype connected to the *SAH* system.

On the glass side, the prototype box is linked via a pipe. In order to discover the behavior of our *SAH* system, we measured the temperature and the air velocity at different regulated points. In fact, to calculate the air velocity, we used the *AM 4204* hot-wire anemometer because it is easy to use and can provide the greatest versatility of use and a high resolution. By reducing the probe to the appropriate location, the speed value can be read directly from the digital screen. Then, to calculate the temperature, we used the Uni-Trend Model *UT325* Thermometer, which is a digital thermometer designed to use external thermocouples of types *J, K, T, E, R, S,* and *N* as the temperature sensors. This system has software and a USB data cable included in the shipment, which helps the thermometer be linked to our laptop and the data will be continuously transmitted. The geometrical structure of the computational domain is shown in figure 2, which consists of two domains separated by a circular pipe with a diameter of $d=100\ mm$. Then, a solar air heater with a height of $h_s=194\ mm$ and a width of $W_s=778\ mm$ is the first. On the other hand, a piece of glass *1000 mm* the long is hung on the front side of this device and an absorber with a length of $L_a=1086\ mm$ is inserted inside. Then, hot airflow is then redirected to the box prototype with a height of $H_b=1100\ mm$, a length of $L_b=1500\ mm$, and width of $W_b=1000\ mm$. On the same side of the box prototype, two circular holes with a distance of $h_2=900\ mm$ are found. The inlet opening,

which is located at a height of $h_1=250\ mm$ and a length of $L_1=300\ mm$, is used to supply the hot air while the outlet opening helps it to escape into the surrounding atmosphere.

Numerical Model

Mathematical Formulation

The modeling airflow is governed by the continuity equation, the momentum equations, the turbulence equations and the energy equation [28-33]. Substituting expressions into instantaneous equations, and taking time average yields, we can write in the Cartesian system the continuity and the momentum equations as follows:

$$\frac{\partial \rho}{\partial t}+\frac{\partial}{\partial x_i}(\rho u_i)=0 \tag{1}$$

$$\frac{\partial}{\partial t}(\rho u_i)+\frac{\partial}{\partial x_j}(\rho u_i u_j)=-\frac{\partial p}{\partial x_i}+\frac{\partial}{\partial x_j}\left[\mu\left(\frac{\partial u_i}{\partial x_j}+\frac{\partial u_j}{\partial x_i}-\frac{2}{3}\delta_{ij}\frac{\partial u_i}{\partial x_i}\right)\right]+\frac{\partial}{\partial x_j}(-\rho\overline{u_i'u_j'}) \tag{2}$$

Where u_i is the velocity components ($m.s^{-1}$), u_j is the velocity components ($m.s^{-1}$), x_i and x_j are the Cartesian coordinates (m), p is thepressure (Pa), t is the time (s), μ is the dynamic viscosity ($Pa.s$) and ρ is the density ($kg.m^{-3}$).

These equations are the *RANS* (Reynolds-averaged Navier-Stokes) equations, which present the same form as the instantaneous equations. The new terms introduce the Reynolds stresses $-\rho\overline{u_i'u_j'}$ should be modeled to close the *RANS* equations.

The used method applies the Boussinesq hypothesis relating the Reynolds stresses with the mean velocity gradients:

$$-\rho\overline{u_i'u_j'}=\mu_t\left(\frac{\partial \mu_i}{\partial x_j}+\frac{\partial \mu_j}{\partial x_i}\right)-\frac{2}{3}\left(\rho k+\mu_t\frac{\partial \mu_k}{\partial x_k}\right)\delta_{ij} \tag{3}$$

This hypothesis is undertaken in different turbulence models. This approach presents a low computational cost compared to another numerical method.

By using the standard k-ω turbulence model, the turbulent viscosity μ_t is defined by:

$$\mu_t=\alpha^*\frac{\rho k}{\omega} \tag{4}$$

Where k is the turbulent kinetic energy ($m^2.s^{-2}$) and ω is the specific dissipation rate (s^{-1}).

For the correction of the low-Reynolds number, α^* is calculated as follows:

$$\alpha^*=\alpha^*_\infty\left(\frac{\alpha^*_0+Re_t/R_k}{1+Re_t/R_k}\right) \tag{5}$$

Where:

$$Re_t=\frac{\rho k}{\mu\omega} \tag{6}$$

$$R_k=6 \tag{7}$$

$$\alpha^*_0=\frac{\beta_i}{3} \tag{8}$$

$$\beta_i=0.072 \tag{9}$$

However, for the high-Reynolds number form of the k-ω model:

$$\alpha^*=\alpha^*_\infty=1 \tag{10}$$

Where Re is the Reynolds number (dimensionless), R_k is theconstant of the k-ω turbulence model (dimensionless), u_i' and u_j' are the fluctuating velocity components ($m.s^{-1}$), μ_t is the turbulent viscosity ($Pa.s$), α_0 and β_1 are the constants of the k-ω turbulence model (dimensionless) and x_k is the Cartesian coordinate (m).

For the low-Reynolds number, the standard *k-ω* turbulence model incorporates modifications. With this model, the turbulent kinetic energy *k* and the specific dissipation rate *ω* are written as follows:

$$\frac{\partial}{\partial t}(\rho k)+\frac{\partial}{\partial x_i}(\rho k u_i)=\frac{\partial}{\partial x_i}\left(\Gamma_k \frac{\partial k}{\partial x_j}\right)+G_k-Y_k+S_k \tag{11}$$

$$\frac{\partial}{\partial t}(\rho \omega)+\frac{\partial}{\partial x_i}(\rho \omega u_i)=\frac{\partial}{\partial x_j}\left(\Gamma_\omega \frac{\partial \omega}{\partial x_j}\right)+G_\omega-Y_\omega+S_\omega \tag{12}$$

Where G_k is thegenerationof the turbulent kinetic energy ($kg.m^{-1}.s^{-3}$), G_ω is the generation of the dissipation rate of the turbulent kinetic energy ($kg.m^{-1}.s^{-3}$), S_k is the source term of the turbulent kinetic energy ($kg.m^{-1}.s^{-3}$), S_ω is the source term of the specific dissipation rate of the turbulent kinetic energy ($kg.m^{-1}.s^{-3}$), Y_ω is the turbulence dissipation of ω ($kg.m^{-1}.s^{-3}$), Γ_k is the effective diffusivity of *k* (*Pa.s*) and Γ_ω is the effective diffusivity of ω (*Pa.s*).
Constants of the standard *k-ω* turbulence model are presented in table 1.

Tab.1 Standard *k-ω* turbulence model constants.

α_0	α_∞	α^*_∞	R_ω	R_k	σ_k	σ_ω
1/9	1.9	1.0	2.95	6.0	2.0	2.0

By using the concept of the Reynolds analogy, the energy equation is written as follows:

$$\frac{\partial}{\partial t}(\rho E)+\nabla\left(\vec{v}(\rho E+p)\right)=\nabla\left(k_{eff}\nabla T-\sum_j h_j \vec{J}_j+(\bar{\bar{\tau}}\vec{v})\right)+S_h \tag{13}$$

Where:
K_{eff} is the effective conductivity $(k+k_t)$, k_t is the turbulent thermal conductivity, $\vec{J}_j$ is the diffusion flux of species *j* and $\left(\tau_{ij}\right)_{eff}$ is the deviatoric stress tensor, defined as follows:

$$\left(\tau_{ij}\right)_{eff}=\mu_{eff}\left(\frac{\partial u_j}{\partial x_i}+\frac{\partial u_i}{\partial x_j}\right)-\frac{2}{3}\mu_{eff}\frac{\partial u_k}{\partial x_k}\delta_{ij} \tag{14}$$

Where u_i is the first velocity component ($m.s^{-1}$), u_j is the second velocity component ($m.s^{-1}$), u_k is the third velocity component ($m.s^{-1}$), x_i is the first Cartesian coordinate (m), x_j is the second Cartesian coordinate (*m*), x_k is the third Cartesian coordinate (*m*), δ_{ij} is the Kronecker delta function (dimensionless) and μ_{eff} is the effective viscosity (*Pa.s*).

Boundary Conditions

Figure 2 demonstrates the boundary conditions of the solar air heater test. In the first hole, the heat flow supplies the box prototype from the outside air heater, the airflow is evacuated from the second hole of the box prototypes, where the inlet and the outlet pressure, a value of $p=101325\ Pa$ was set.

The others side surfaces of the box prototype are assumed as walls surrounding the computational domain. In these surfaces, Dirichlet boundary conditions are imposed and admit these values $V=0\ m.s^{-1}$ and $T=290\ K$. Moreover, we have specified all the considered parameters of the radiation model under fair weather conditions using the solar calculator of the Discrete Ordinates (*DO*). In these conditions, the longitude, the latitude, and the time zone for the global location are added. Indeed, the day, the month, the hour, and the minute for the date and time are indicated. In addition, the north and the east of the mesh orientation are defined.

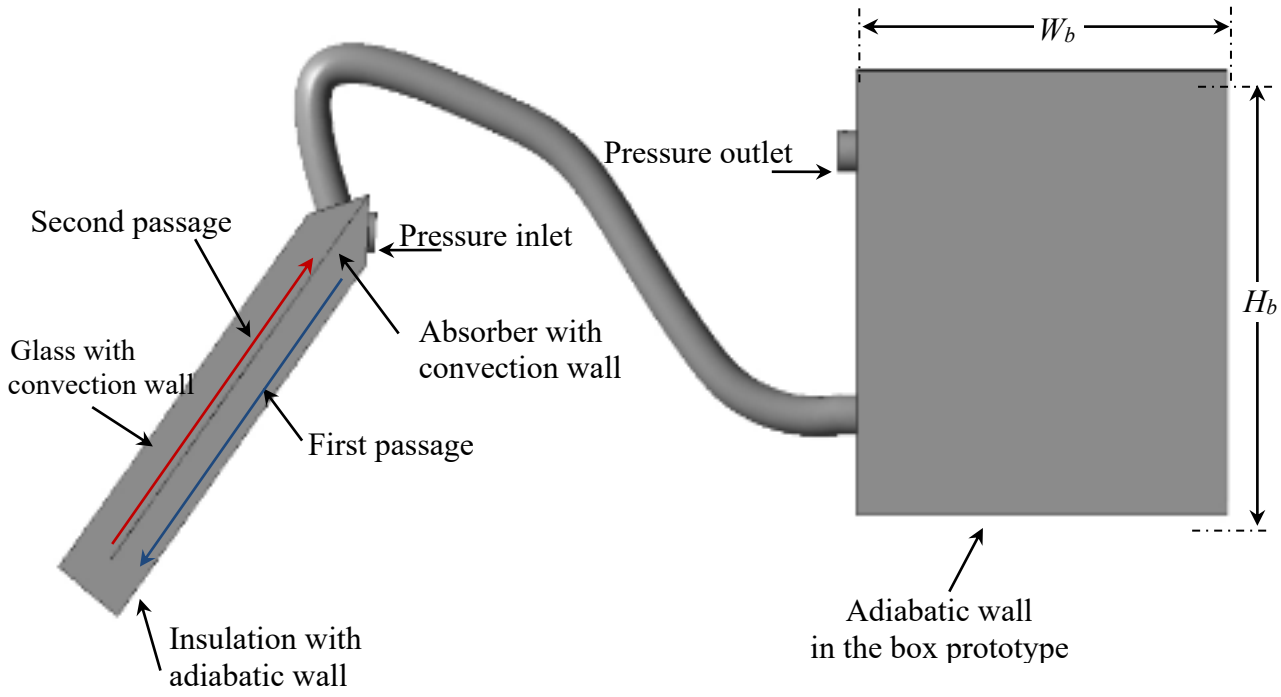

Fig.2 View of the solar air heater test bench.

Meshing

The elaborated mesh was developed with unstructured and tetrahedral meshing using commercial software ANSYS *17.0*, as shown in figure 3. In the current application, we have set up a refined model made of a number of cells having a lower numerical diffusion equal to *N=1578369* cells. Therefore, in order to model our considered application, which refers to the turbulent flow in the solar air heater test bench at *t=12 hours*, we have taken into account the results of the *CFD* with a measurement time equal to *t=10 days*.

In these circumstances, the residual values corresponding to the numerical parameters are equal to 10^{-6}. Besides, in such simulations, the used computer is characterized by an Intel *(R) Xeon (R) CPU E3-1226v3 @ 3.30 GHz cpu*, *12.0 GB* of installed memory (RAM) (usable *11.7 GB*), and a *64-bit* operating system of *x64 cpu* processor.

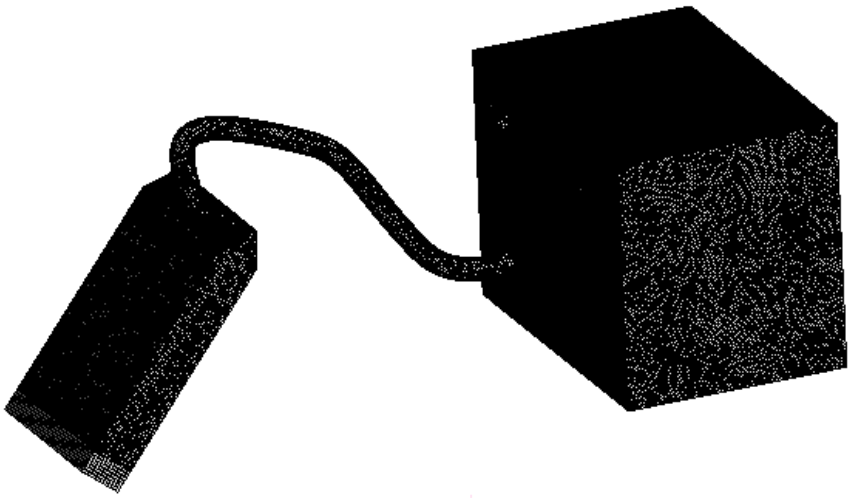

Fig.3 Meshing of the computational domain.

Results and Discussion

This section presents the distribution of the velocity field, the temperature, the total pressure, the turbulent kinetic energy, and the turbulent viscosity. Then, the Reynolds number, equal to *Re=1300*, is assessed.

Velocity fields

For the first and second passages of the solar air heater supplying the box prototype, figure 4 shows the distribution of velocity fields in the various longitudinal and transverse planes. In fact, based on these findings, it is obvious that the inlet velocity has a poor value equal to $V=0.2\ m.s^{-1}$. At the first passage, an increase in the hot air flow was observed in the first passage of the solar air heater. At the beginning of the flow, a maximum value equal to $V=0.5m.s^{-1}$ was noticed while the velocity decreases steadily from the center of the first passage of the solar air heater until the solar air heater hits the bottom. At this stage, the velocity has a value equal to $V=0.15\ m.s^{-1}$. In fact, along the second passage of the solar air heater, various recirculation zones are observed. However, at this stage, the very small velocity is evaluated at around $V=0.5m.s^{-1}$, which exceeds $V=0.25\ m.s^{-1}$ by crossing the pipe separating the solar air heater from the box prototype. On the other hand, the reverse wall is occupied by a discharge area through the box prototype inlet holes. Then, the speed alters its course on this side, and two axial flows can be observed. The first upward flow is responsible for the recirculation zone, which emerged in the box prototype region as a whole. In fact, this motion continues through the hole outlet until the airflow exits and reaches a maximum value equal to $V= 0.23\ m.s^{-1}$. Then, the second downward flow is due to the emergence of a dead zone in the lower region. Globally, the average velocity value in the discharge region is about $V=0.1\ m.s^{-1}$.

Physically, these results confirm that the hot zone is created on the mirror side receiving the solar radiation. It generates an ascendant movement that goes from the bottom to the top and enters the box prototype. The same phenomenon has been observed in the box where the airflow coming from the solar heat escapes into the environment. This movement created between the hot zone of the solar heat and the box prototype is also imposed in the cold zone of the solar heat on the heat-insulating side. In these conditions, the air movement flows from the top to the bottom. Indeed, the acceleration of the air velocity at the inlet of the solar heat is due to the change of the section which is more reduced by comparison to the rest of the air circulation duct.

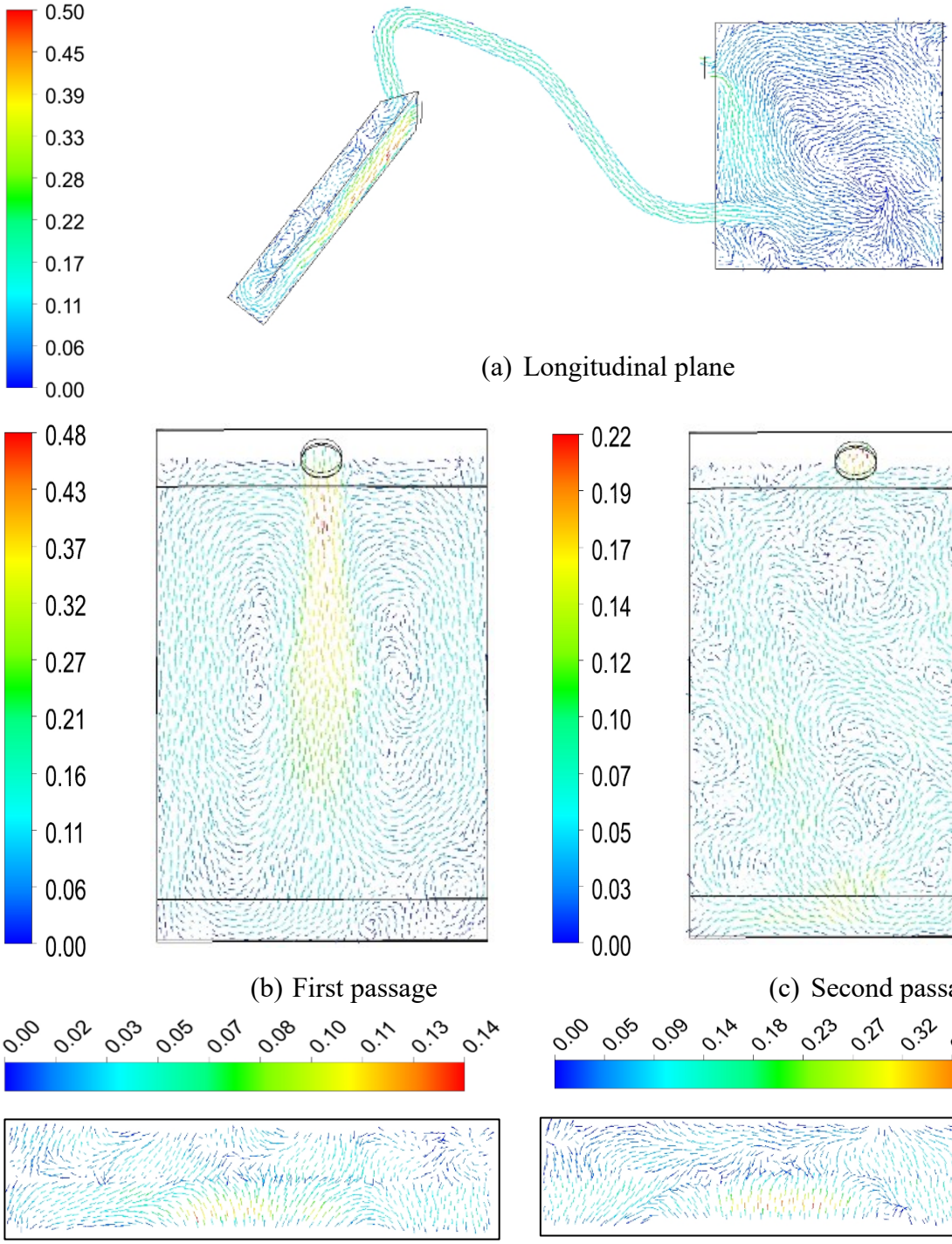

Fig.4 Distribution of the velocity field.

Temperature

For the first and second passages of the solar air heater supplying the box prototype, figure 5 shows the temperature distribution in the various longitudinal and transverse planes. Based on these results, the temperature of the inlet is regulated by the boundary condition described by $T=308\ K$. However, this value increases tremendously to reach an average value equal to $T=339\ K$ in the first passage and $T=345\ K$ in the second passage.

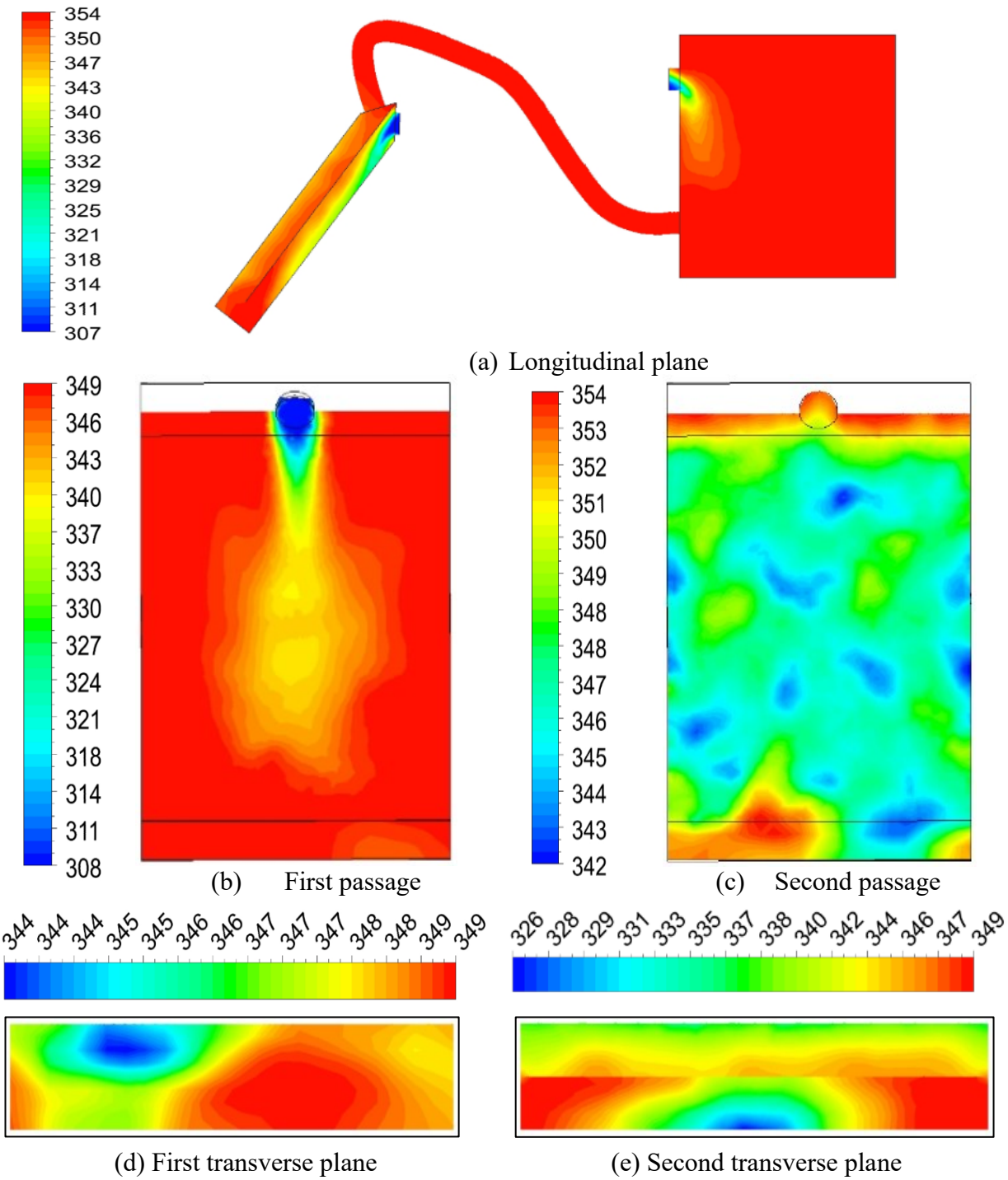

Fig.5 Distribution of the total temperature.

This reality can be explained by the fact that the airflow reaches the surrounding temperature then passes through the channel between the absorber plate and the insulation and starts to swarm with the absorber through convection. In the second passage, as the flow between the glass and the absorber is affected by solar radiation, the temperature of the flowing air is more significant. Then, the box prototype is operated by a continuous air heater characterized by a maximum temperature value equal to $T=349\ K$, which decreases to reach $T=308\ K$ in the outlet hole of the box prototype.

Physically, these results are confirmed since the hot zone is localised on the mirror side which receives the solar radiation. However, the cold zone is on the other side opened to the ambient environment constituting the cold source. Under this movement, the box prototype constitutes the environment that stores the heat from its entry and escapes it from its exit.

Total pressure

Regarding the first and second passages of the solar air heater supplying the box prototype, figure 6 shows the overall pressure distribution in the various longitudinal and transverse planes.

Based on these results, it is obvious that the pressure inlet is controlled by the frontier condition identified by the atmospheric pressure of $p=101325\ Pa$. On the other hand, the total pressure at the bottom of the solar air heater drops and reaches $p=101324\ Pa$.

From this side of the solar air heater, the overall pressure in the second passage significantly increases while the cumulative pressure at the exit of the second passage begins to rise along the pipe to reach a value equal to $p=101326\ Pa$ in the first half of the pipe separating the solar air heater from the prototype box. In fact, there is a slight improvement from the box prototype roof hole inlet.

Indeed, there is a small rise in the overall pressure from the inlet hole of the box prototype roof to the box prototype roof. The maximum value of the cumulative pressure on this side, which is equal to $p=101326\ Pa$, is controlled in the outlet hole of the box prototype by the frontier condition specified by the atmospheric pressure with $p=101325\ Pa$.

These obtained results confirm the physical phenomenon found in the velocity and temperature distributions. In fact, the difference in the pressure between the outlet of the solar heat and the inlet of the box prototype leads to the movement of air and its global circulation direction. The depression zone created below the solar air heater is responsible on the admission of the air from the hole placed on the heat-insulating side. Indeed, the compression zone created on the top of the box prototype explains the exhaust of the air from the hole placed on the meet of the external environment.

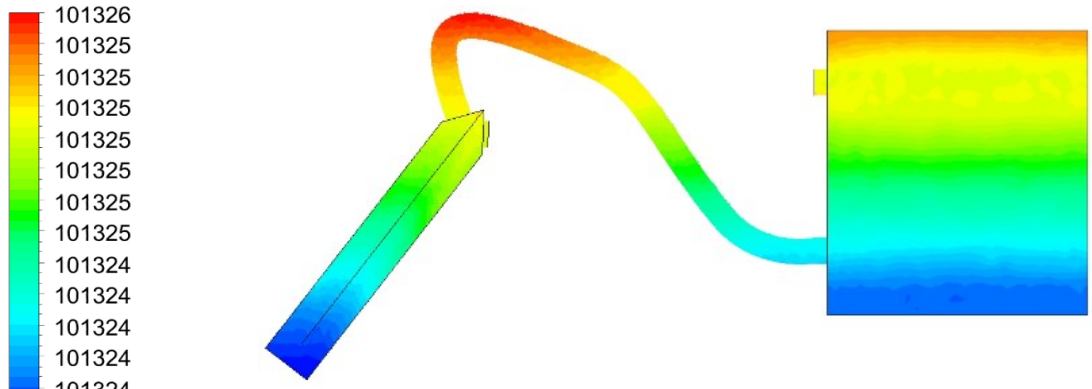

(a) Longitudinal plane

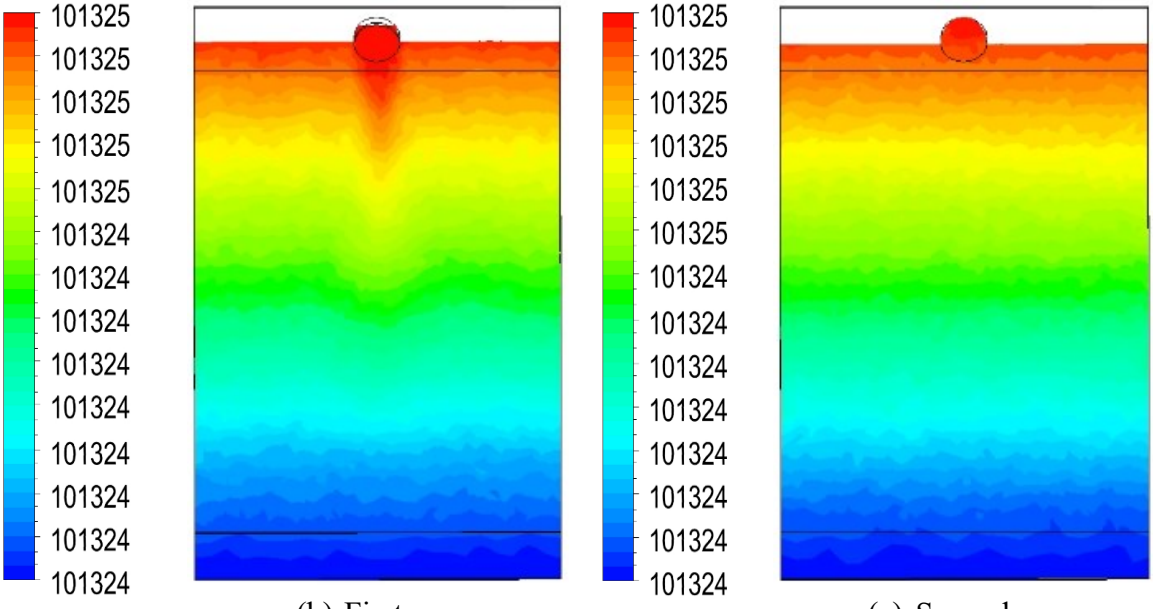

(b) First passage (c) Second passage

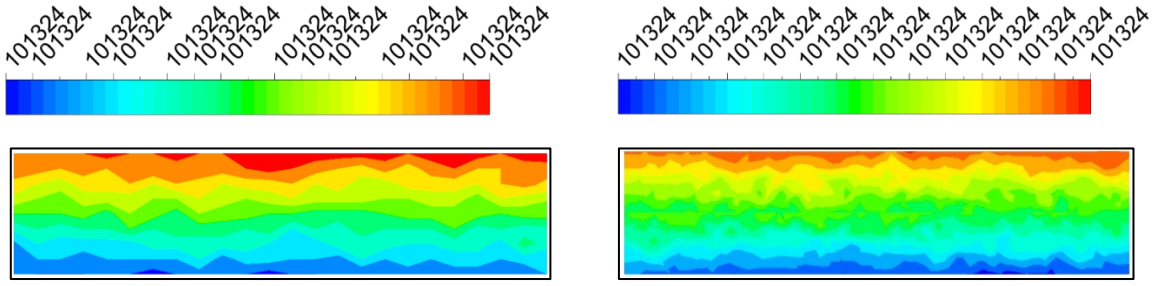

(d) First transverse plane (e) Second transverse plane

Fig.6 Distribution of the total pressure.

Turbulent kinetic energy

For the first and second passages of the solar air heater supplying the box prototype, figure 7 shows the turbulent kinetic energy distribution in the separate longitudinal and transverse planes. According to these findings, the turbulent kinetic energy in the collector inlet of a solar air heater shows a poor value. Then, the turbulent kinetic energy rises during the first passage to reach its maximum value at the second mid-plane and near the absorber. On the other hand, the maximum value of the turbulent kinetic energy on this side is equal to $k = 0.1\ m^2.s^{-2}$. After that, the turbulent kinetic energy drops at the exit hole of the first passage before rising in the second passage.

The maximum value equal to $k=0.19\ m^2.s^{-2}$ implies that the turbulent kinetic energy value decreases at the exit of the first passage and becomes very weak. In fact, two small wake zones characterizing the maximum values of the turbulent kinetic energy are observed with some variance as the flow progresses within the pipe. Then, the expulsion zone in the discharge region is occupied at the inlet hole of the box prototype before the reverse wall is reached. Below the prototype box and in the outlet holes, the wake zone characterizing the maximum value of the turbulent kinetic energy is observed at a value equal to $k=0.07\ m^2.s^{-2}$.

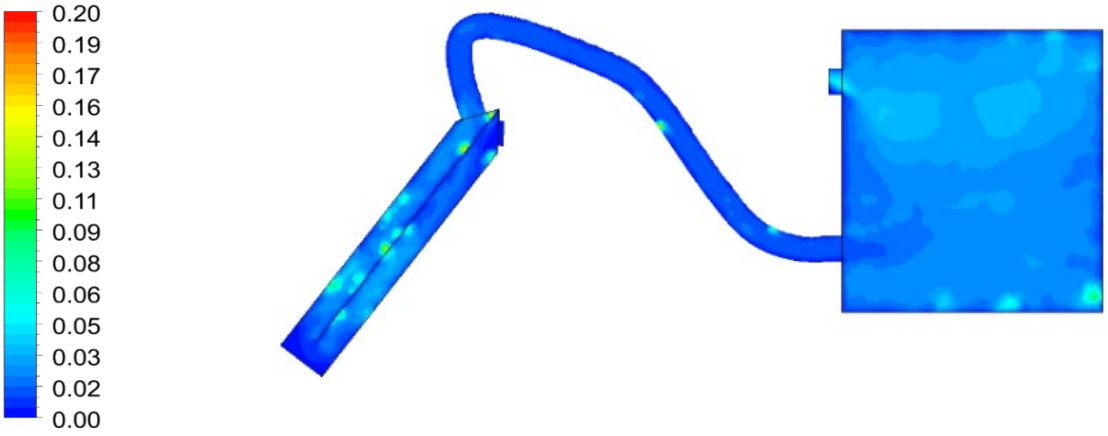

(a) Longitudinal plane

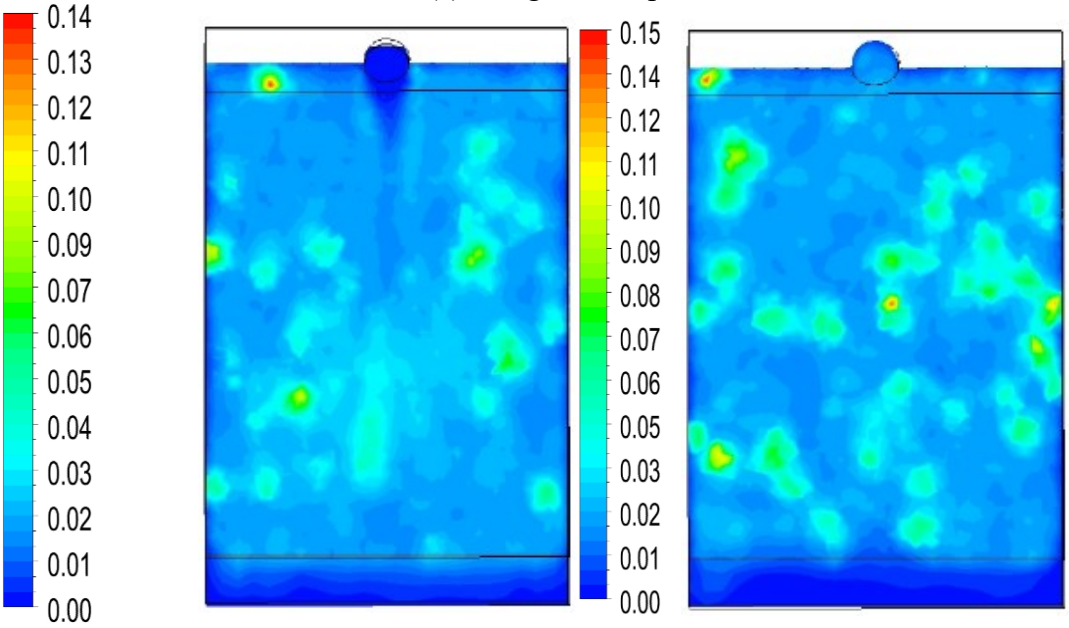

(b) First passage (c) Second passage

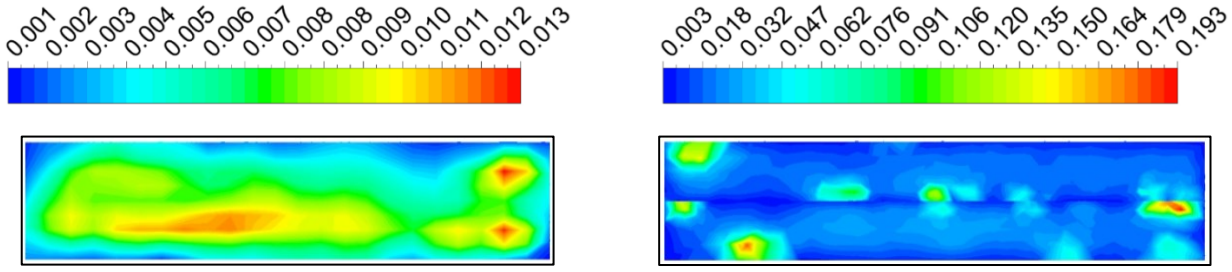

(d) First transverse plane (e) Second transverse plane

Fig.7 Distribution of the turbulent kinetic energy.

Turbulent viscosity

Regarding the first and second passages of the solar air heater supplying the box prototype, figure 8 shows the turbulent viscosity distribution in the various longitudinal and transverse planes. At the collector inlet of the solar air heater, there is a poor value of the turbulent viscosity. On the other hand, behind this zone, a wake one characterizing the maximum value of the turbulent viscosity was observed and extended in the first passage near the absorber extremity.

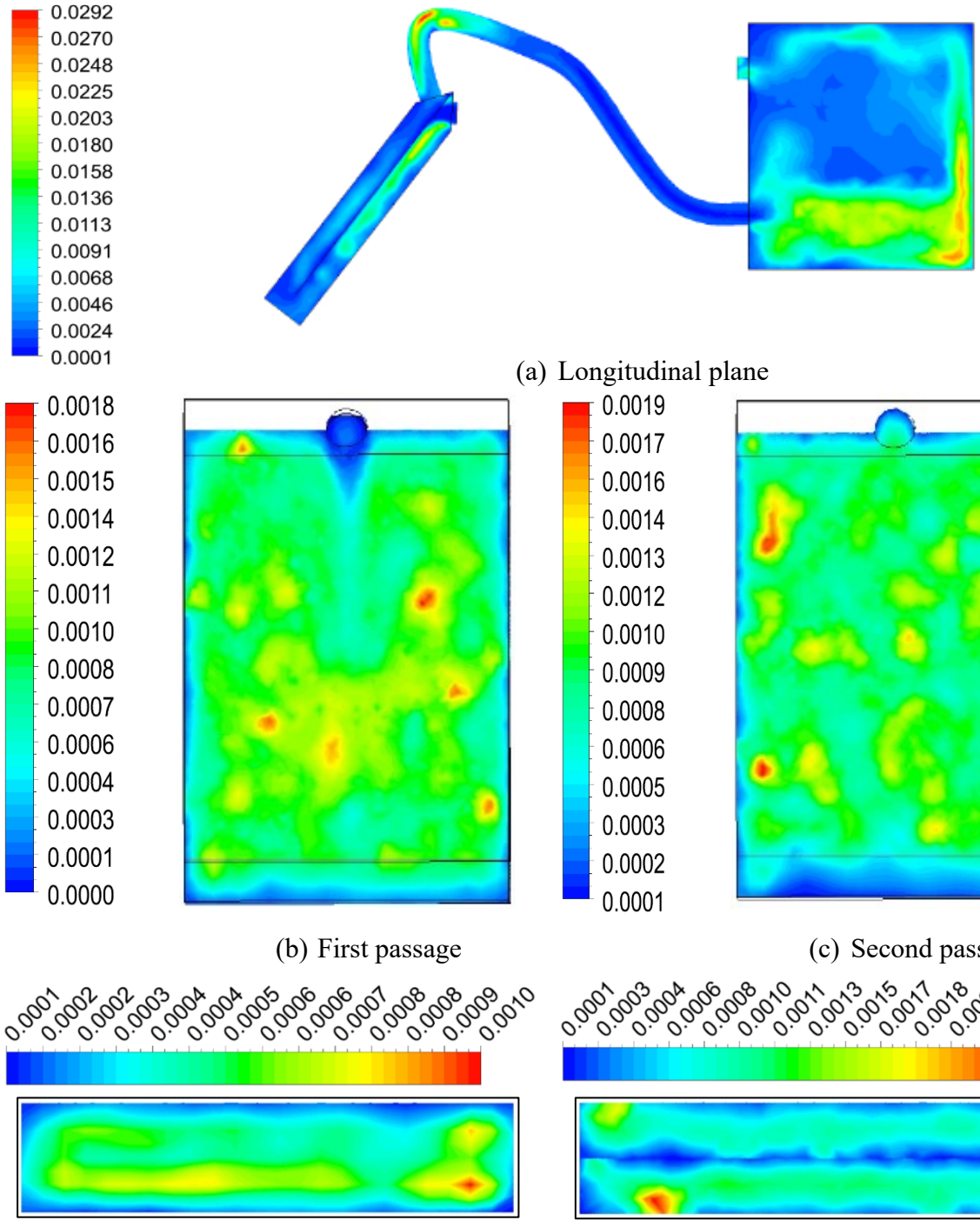

Fig.8 Distribution of the turbulent viscosity.

In fact, the maximum value of the turbulent viscosity in these conditions is equal to $\mu_t=0.022\ kg.m^{-1}.s^{-1}$, which implies that away from this zone, turbulent viscosity shows a very weak value. The same thing is found in the second passage where the maximum value is equal to $\mu_t=0,009\ kg.m^{-1}.s^{-1}$ in the first mid-plane, which means that the turbulent viscosity of the absorber has a poor value. However, at the end of the second passage, the turbulent viscosity slightly rises to reach $\mu_t=0.029\ kg.m^{-1}.s^{-1}$ in the first part of the pipe connecting the solar air heater to the box prototype. In the remaining tubing, the turbulent viscosity drops and records very low values, which appear in the hole inlet of the box prototype in the first half of the discharge zone whereas, in the second half, the turbulent viscosity rises slightly on the side of the reverse wall. Moreover, the turbulent viscosity has a poor value in the rest of the box prototype zone, which can be

demonstrated by the wake zone in the whole zone of the box prototype. In fact, in the upper prototype box and the outlet hole, the turbulent viscosity increases slightly to reach $\mu_t=0.011\ kg.m^{-1}.s^{-1}$.

Validation of the numerical process

Figure 9 compares the numerical results of the superimposed second channel temperature and the velocity profiles as well as our experimental results in the natural convection mode. In fact, the main monitored line of the heated airflow evacuated from the outlet of the *SAH* device holes represents the chosen path. Based on these observations, it is obvious that at the entrance of the second passage of the *SAH* system, the temperature reaches $T=348\ K$. Then, it rapidly drops to $T= 345\ K$ while at the glass side of the airflow direction, it remains constant. Near the hole outlet of the *SAH* system, this temperature rises to hit $T=349\ K$. As for the velocity profile, it is observed that at the entrance of the second passage of the SAH system, the velocity magnitude is around $V=0.15\ m.s^{-1}$ then drops to $V=0.05\ m.s^{-1}$.With the exception of the hole outlet, it maintains this value along the second passage. In fact, the velocity of magnitude increases tremendously at this stage as it exceeds $V=0.2\ m.s^{-1}$. Moreover, a similar appearance has been globally observed between the curves of the experimental and numerical effects. In fact, the difference between the curves is around *6 %.* This slight mismatch can be related to the perturbations that can be occurred in experiments when we insert the probe to measure the velocity. This disturbance is expected at the local level but it does not change the overall structure of the flow as well as the system functioning. Never the less, the global trend of both curves presents a good agreement and validates the numerical method.

By referring to the classic solar air heater with one passage, we found that the energy efficiency measured in the same conditions gives enhanced performance and presents the efficient one with an improvement of about *27%*. These results can be confirmed in the paper of Elsanossi [27] referring to the performance analysis of a solar air heater with different absorber materials in a single pass.

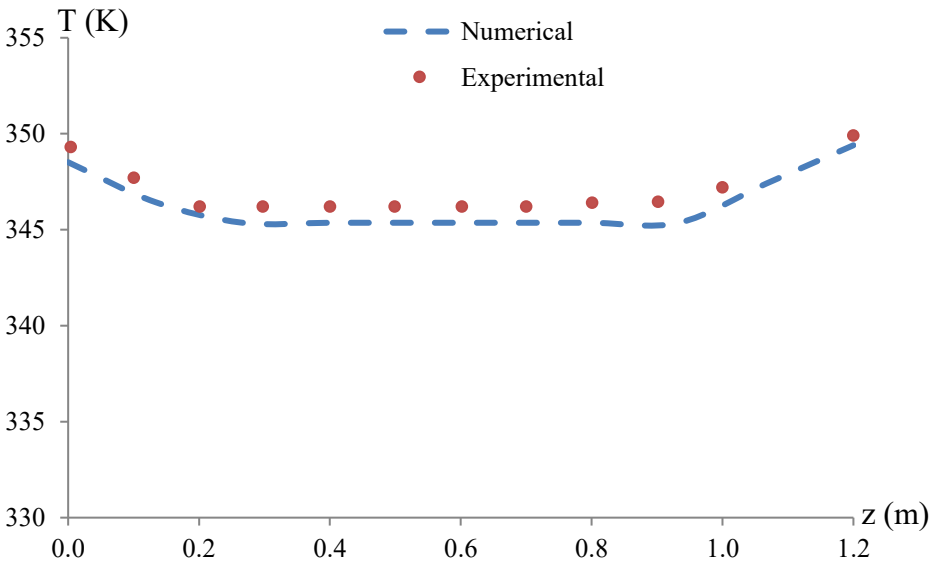

(a) Temperature profile

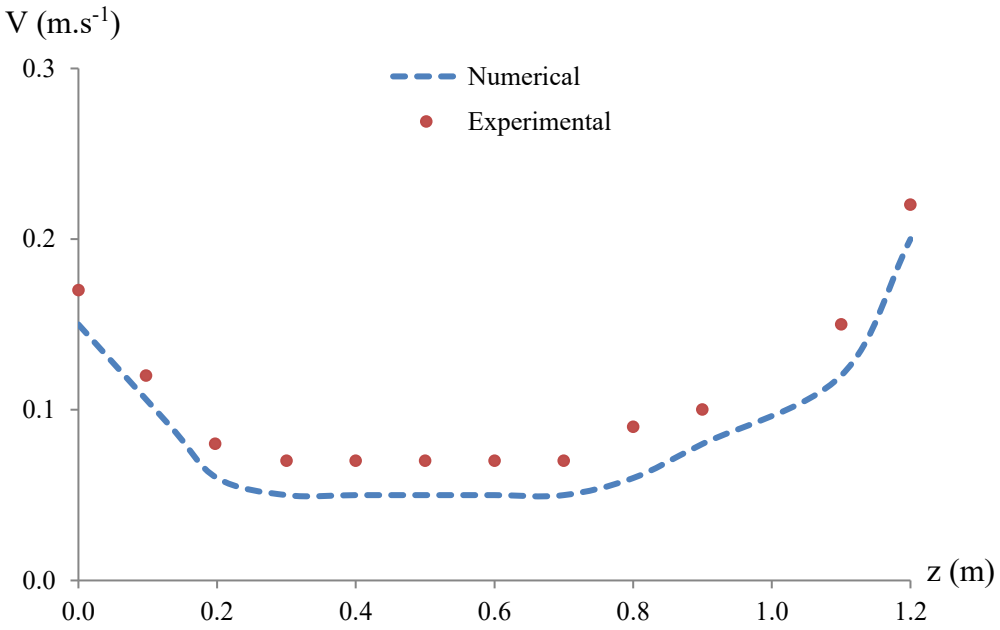

(b) Velocity profile

Fig.9 Comparison with experiments.

Conclusion

The most important technology, which is not very widely used in domestic and industrial applications, is heating the air with a solar heater. For this reason, we are interested in designing and implementing a new solar air heater test bench to investigate the solar system performance. The device in question consists of two passages of solar air heater separated by an absorber with natural convection on the insulation side. It is linked to the box prototype on the glass side via a pipe. Indeed, we have built numerical simulations to characterize the aero-thermal structure of our new system operating in natural convection. In these conditions, it has been observed that the hot zone created on the mirror side receiving the solar radiation generates an ascendant movement. It goes from the bottom to the top and enters the box prototype. The same phenomenon is also created in the box where the airflow coming from the solar heat escapes into the environment. This movement created between the hot zone of the solar heat and the box prototype is also imposed in the cold zone of the solar heat on the heat-insulating side. In these conditions, the air movement is however from the top to the bottom. Indeed, the acceleration of the air velocity at the inlet of the solar heat is due to the change of the section which is more reduced by comparison to the rest of the air circulation duct. Based on our experimental results generated in a two-passage solar air heater connected to the box prototype, the computational approach and the simulation results were validated. By referring to the classic solar air heater with one passage, the energy efficiency measured in the same conditions was enhanced and presented the efficient one with an improvement of about *27%*.

This technology would be very useful and is recommended since it can provide renewable energy and can substitute costly conventional technologies.

Nomenclature

SAH	Solar air heaters
k–ω	The standard turbulence model
CFD	Computational fluid dynamics
DME	Dimethyl ether

LS-SVM	Square support vector machine
ANN	Artificial neural network
WNN	The wavelet neural network
J, K, T, E, R, S and N	External thermo couples
D	Diameter (mm)
h_s, h_1, h_2	Height (mm)
W_b , W_s, W_b	Width (mm)
L_1, L_b , L_a	Length(mm)
RANS	Reynolds-averaged Navier-Stokes
DO	The Discrete Ordinates
N	Number of cells
A_0	Model constant
A_s	Model constant
C_1	Model constant
E	Total energy (J)
F_i	Forcecomponentsonthe i direction (N)
G_k	Generationof the turbulent kinetic energy ($kg.m^{-1}.s^{-3}$)
G_ω	Generation of the dissipation rate of the turbulent kinetic energy ($kg.m^{-1}.s^{-3}$)
H	Height (m)
H	Thermal enthalpy ($J.kg^{-1}$)
K_{eff}	Effective conductivity ($W.m^{-1}. K^{-1}$)
K	Turbulent kinetic energy ($m^2.s^{-2}$)
k_t	The turbulent thermal conductivity
$\vec{J}_j$	The diffusion flux of species j
l	Length (m)
p	Pressure (Pa)
P_r	Prandt number (dimensionless)
Q_H	Heat source or sink per unit volume ($kg.m^{-1}.s^{-3}$)
q_i	Diffusive heat flux (J)
Re	Reynolds number (dimensionless)
R_k	Constant of the k-ω turbulence model (dimensionless)
R_ω	Constant of the k-ω turbulence model (dimensionless)
S	Scalar measure of the deformation tensor (dimensionless)
S_i	Mass-distributed ($kg.m^{-2}.s^{-2}$)
S_{ij}	Mean rate-of-strain tensor (s^{-1})
S_ω	Source terms of the specific dissipation rate of the turbulent kinetic energy ($kg.m^{-1}.s^{-3}$)
S_k	Source terms of the turbulent kinetic energy ($kg.m^{-1}.s^{-3}$)
T	Temperature (K)
t	Time (s)
U	Velocity components ($m.s^{-1}$)
$u_i^{'}$	Fluctuating velocity components ($m.s^{-1}$)
u_i , u_j, u_k	The velocity components ($m.s^{-1}$),
Ω	The specific dissipation rate
V	Magnitude velocity ($m.s^{-1}$)

x_k, x_i, x_j	Cartesian coordinate (m)
X	Cartesian coordinate (m)
Y	Cartesian coordinate (m)
Y_M	Fluctuating dilatation in compressible turbulence ($kg.m^{-1}.s^{-3}$)
Y_k	Turbulence dissipation of k ($kg.m^{-1}.s^{-3}$)
Y_ω	Turbulence dissipation of ω ($kg.m^{-1}.s^{-3}$)
Z	Cartesian coordintate (m)
U	Free-stream velocity (m/s)
α_0	Constant of the k-ω turbulence model (dimensionless)
α_∞	Constant of the k-ω turbulence model (dimensionless)
$\alpha^*, \alpha^*_\infty$	Constant of the k-ω turbulence model (dimensionless)
δ_{ij}	Kronecker delta function (dimensionless)
M	Dynamic viscosity (Pa.s)
μ_t	Turbulent viscosity (Pa.s)
μ_{eff}	Effective viscosity (Pa.s)
ω	Specific dissipation rate (s^{-1})
P	Density ($kg.m^{-3}$)
β_I	Constant of the k-ω turbulence model (dimensionless)
σ_k	Turbulent Prandtl number for k (dimensionless)
σ_ω	Turbulent Prandtl number for ω (dimensionless)
τ_{ij}	Viscous shear stress tensor (Pa)
$(\tau_{ij})_{eff}$	Deviatoric stress tensor (Pa)
Φ	Equivalence ratio (dimensionless)
Γ_k	Effective diffusivity of k (Pa.s)
Γ_ω	Effective diffusivity of ω (Pa.s)
Ω	Swirl number (dimensionless)
Ω_{ij}	Rate of rotation tensor (s^{-1})

References

[1] J.S. David, J. Viveckraj, S. Sivamani, K. Varatharajan, Comparative study of solar water heating systems - flat plate collector (FPC) with evacuated Tube Collector, Int. J. Eng. Res. Africa. 26 (2016) 76-85.

[2] S. Ravishankar, P.K. Nagarajan, D. Vijayakumar, Experimental validation of fresh water production using triangular pyramid solar still with PCM storage, Int. J. Eng. Res. Africa. 20 (2016) 51-58.

[3] C. Khelifi, F. Ferroudji, M. Ouali. Analytical Modeling and Optimization of a solar chimney power plant, Int. J. Eng. Res. Africa. 25 (2016) 78-88.

[4] D. Taloub, A. Bouras, Z. Driss. effect of the soil inclination on natural convection in half-elliptical green houses, Int. J. Eng. Res. Africa. 50 (2020) 70-78.

[5] B. Bakri, O. Eleuch, A. Ketata, S. Driss, Z. Driss, H. Benguesmia, Study of the turbulent flow in a newly solar air heater test bench with natural and forced convection modes, Energy.161 (2018) 1028-1041.

[6] A.K. Pandey, M. Kumar, Natural convection and thermal radiation influence on nanofluid flow over a stretching cylinder in a porous medium with viscous dissipation, Alexandria Eng. J., 56 (2017) 55–62.

[7] P. Singh, A.K. Pandey, M. Kumar, Forced convection in MHD slip flow of alumina-water nanofluid over a flat plate, J. Enh. H. Trans. 23 (2016) 487- 497.

[8] Z. Bocu, Z. Altac, Laminar natural convection heat transfer and air flow in three dimensional rectangular enclosures with pin arrays attached to hot wall, App. Therm. Eng. 31 (2011) 3189–3195.

[9] A.A. El-Sebaii, S. Aboul-Enein, M.R.I. Ramadan, S.M. Shalaby, B.M. Moharram, Thermal performance investigation of double pass-finned plate solar airheater, App. En. 88 (2011)1727–1739.

[10] M.A. Wazed, Y. Nukman, M.T. Islam, Design fabrication of a cost effective solar air heater for Bangladesh, App. En, 87(2010)3030–3036.

[11] K. Sopian, M.A. Alghoul, M.A. Ebrahim, M.Y. Sulaiman, E.A. Musa, Evaluation of thermal efficiency of double-pass solar collector with porous- nonporousmedia, Ren. En. 34 (2009) 640-645.

[12] H. Esen, Experimental energy and exergy analysis of a double-flow solar airheater having different obstacles on absorber plates, Buil. Env.43 (2008) 046-1054.

[13] F. Ozgen, M. Esen, H. Esen, Experimental investigation of thermal performanceof a double-flow solar air heater having aluminum cans, Ren. En, 34 (2009)2391-2398.

[14] C. Teodosiu, F. Kuznik, R. Teodosiu, CFD modeling of buoyancy driven cavities with internal heat source: Application to heated rooms, En. Buil.68 (2014) 403-411.

[15] S. Driss, Z. Driss, I. Kammoun, Computational study and experimental validation of the heat ventilation in a living room with a solar patio system, En. Buil.119 (2016) 28-40.

[16] S. Driss, Z. Driss, I. Kammoun, Numerical simulation and wind tunnel experiments on wind-induced natural ventilation in isolated building with patio, Energy. 90 (2015) 917-925.

[17] N. Joshi, A. K. Pandey, H. Upreti, M. Kumar, Mixed convection flow of magnetic hybrid nanofluid over a bidirectional porous surface with internal heat generation and a higher-order chemical reaction, H. Trans. 50 (2020) 3661–3682.

[18] H. Hassan, S. Abo-Elfadl, Experimental study on the performance of double pass and two inlet ports solar air heater (SAH) at different configurations of the absorber plate, Ren. En. 116 (2018) 728-740.

[19] T. Alam, M-H. Kim, Performance improvement of double-pass solar air heater–A state of art of review, Ren. Sust. En. Rev.79 (2017) 779-793.

[20] M. Goodarzi, E. Nouri, A new double-pass parallel-plate heat exchanger with better wall temperature uniformity under uniform heat flux, Int. J. Therm. Sci. 102 (2016)137-144.

[21] S. Singh, P. Dhiman, Thermal performance of double pass packed bed solar air heaters–A comprehensive review, Ren. Sust. En. Rev. 53 (2016) 1010-1031.

[22] L. Chen, X.R. Zhang, Experiments on natural convective solar thermal achieved by supercritical CO2/dimethyl ether mixture fluid, J. Sol. En. Eng. 136 (2014) n° 031011.

[23] X.R. Zhang, Y. Zhang, L. Chen, Experimental study on solar thermal conversion based on supercritical natural convection, Ren. Energy. 62 (2014) 610-618.

[24] L. Chen, X.R. Zhang, Experimental analysis on a novel solar collector system achieved by supercritical CO2 natural convection, En. Conv. Manag. 77 (2014) 173-182.

[25] H. Esen, F. Ozgen, M. Esen, A. Sengur, Modelling of a new solar air heater through least-squares support vector machines, Exp. Sys. Appl. 36 (2009) 10673–10682.

[26] H. Esen, F. Ozgen, M. Esen, A. Sengur, Artificial neural network and wavelet neural network approaches for modelling of a solar air heater, Exp. Sys. Appl. 36 (2009) 11240–11248.

[27] H.I. Elsanossi, Performance analysis of solar air heater with different absorber material in single pass. Int. Res. J. Eng. Tech. 5(2018) 2795-2801.

[28] Z. Driss, O. Mlayeh, D. Driss, M. Maaloul, M.S. Abid, Numerical simulation and experimental validation of the turbulent flow around a small incurved Savonius wind rotor, Energy. 74(2014) 506-517.

[29] Z. Driss, O. Mlayah, S. Driss, D. Driss, M. Maaloul, M.S. Abid, Study of the bucket design effect on the turbulent flow around unconventional Savonius wind rotors, Energy. 89(2015) 708-729.

[30] Z. Driss, O. Mlayah, S. Driss, M. Maaloul, M.S. Abid, Study of the incidence angle effect on the aerodynamic structure characteristics of an incurved Savonius wind rotor placed in a wind tunnel, Energy. 113(2016) 894-908.

[31] B. Bakri, A. Ketata, S. Driss, H. Benguesmia, Z. Driss, F. Hamrit, Unsteady investigation of the heat ventilation in a box prototype, Int. J. Therm. Sci.135(2019) 285–297.

[32] H. Benguesmia, B. Bakri, Z. Driss, A. Ketata, S. Driss, Effect of the turbulence model on the heat ventilation analysis in a box prototype, Diag. 21(2020) 55-66.

[33] B. Bakri, O. Eleuch, A. Ketata, S. Driss, Z. Driss, H. Benguesmia, Study of the turbulent flow in a newly solar air heater test bench with natural and forced convection modes, Energy. 161(2018) 1028-1041.